ARCHIVE OF MECHANICAL ENGINEERING
DOI: 10.24425/ame.2025.154738 2025, Vol. 72, No. 2, pp. 311–332

NGUYEN Van Cuong [1], NGUYEN Van Duong [2], BUI Manh Cuong [1], CHU Manh Hoang [3]

One-axis micro-electromechanical accelerometer with enhanced sensitivity

Received 11 October 2024, **Revised** 4 June 2025, **Accepted** 16 June 2025, **Published online** 3 July 2025

Keywords: one-axis accelerometer, air damping, electrostatic tuning, enhanced sensitivity

Micro-electro-mechanical systems (MEMS)-based sensor technologies are essentially influencing the development of smart sensing applications. The primary reasons are due to their small dimensions, low energy use, and very reasonable prices. This article, for the first time, presents a novel design of a single-axis MEMS acceleration sensor with enhanced sensitivity using electrostatic stiffness softening effect. The novel sensor design has two distinct masses, each serving a unique purpose and fulfilling a specific function. One mass is responsible for sensing vibrations while the other mass is used for tuning resonant frequency. Using the proposed tuning method, the double mass sensor's sensitivity is enhanced by a factor of 18 compared with that of the single mass sensor. The study findings serve as a crucial foundation for the calculation and development of high-performance MEMS acceleration sensors for applications in mechanical oscillation measurements.

1. Introduction

With the development of micro-electro-mechanical systems (MEMS) technology, many micro-sized devices have been created, especially accelerometers [1]. Acceleration sensors are widely used for various applications such as measuring and monitoring ground vibrations with an acceleration value around 0.1g [2], monitoring human health through the detection of tremor, movement disorders in the frequency range of 1–20 Hz [3], or measuring the performance of

✉ CHU Manh Hoang, e-mails: hoangcm@itims.edu.vn, hoang.chumanh@hust.edu.vn
[1]Faculty of Mechanical Engineering, Le Quy Don Technical University, Hanoi, Vietnam
[2]FPT University, Hoa Lac High Tech Park, Hanoi, Vietnam
[3]School of Materials Science and Engineering, Hanoi University of Science and Technology, Hanoi, Vietnam

© 2025. The Author(s). This is an open-access article distributed under the terms of the Creative Commons Attribution (CC-BY 4.0, https://creativecommons.org/licenses/by/4.0/), which permits use, distribution, and reproduction in any medium, provided that the author and source are cited.

tactical and navigation-grade inertial navigation system at frequency of 524 kHz [4]. In general, acceleration sensors' specifications such as sensitivity, frequency response, and resolution are dependent on applications [1–4]. Acceleration sensors work based on several sensitive mechanisms, including capacitive, piezoelectric, piezoresistive, magnetic, and optic sensing mechanisms [1–13].

The capacitive sensing mechanism is one of the most widely used mechanisms due to its high sensitivity, low power consumption, and ability to detect both static and dynamic acceleration. Among capacitive sensing mechanisms, differential capacitive sensing configuration shows ability of reducing noise, especially common-mode noise, leading to clearer and more reliable signal output [6–8]. The majority of current accelerometers are designed with a single mass for measuring z-axis (out-of-plane) or in-plane acceleration [1, 6–8].

Besides accelerometers with a single mass, there are also several studies highlighting the advantages of multi-mass acceleration sensors [14–17]. In Refs. [15, 16], two resonators symmetrically connected to two ends of a proof mass by micro-levers. The proof mass senses external acceleration, while the two resonators form differential resonance measurement. However, the acceleration sensors designed with the two resonators placed on two ends of the proof mass could result in mechanical coupling between the two resonators, potentially limiting operation, particularly when the resonant frequencies are closely matched. With the single resonator design, issues relating to oscillation cross-talk is eliminated [17]. For single mass accelerometers, the center proof mass directly connected to two opposite variable capacitor systems to form differential capacitive change [1, 6–8], while the beam resonator in Ref. [17] connected with two inertial masses through micro-levers, forms differential resonance variation by exciting the resonant beam in the second order transverse mode. In addition, in order to amplify the sensitivity of acceleration sensors, several methods have been proposed such as micro-lever force amplification mechanism [15–18], vacuum package for reducing damping to increase quality factor [19], and electrostatic stiffness softening effect [20]. Compared with the other sensitivity enhancement methods, the tuning method using the electrostatic stiffness softening effect shows the advantages in both enhancing sensitivity and dynamically adjusting sensitivity in real-time without compromising mechanical durability or increasing the device dimension [20].

Furthermore, fabrication tolerances cannot be avoided, leading to differences between the resonant frequency of the sensors after fabrication with the designed value. On the other hand, frequency drift due to the temperature sensitivity of the sensor is also another important issue that needs to be addressed. Therefore, post-fabrication active frequency tuning is necessary. To address this issue, electrostatic tuning method is also employed to tune resonance frequency [21, 22]. Additionally, in the majority of MEMS accelerometers, the moving micro-structures are surrounded by air which significantly affects their dynamics behaviors [23–26]. There are two typical types of air damping in MEMS accelerometers: squeeze-film air damping and slide-film air damping [23]. Squeeze-film air damping and

slide-film air damping are two mechanisms causing energy dissipation in MEMS devices. Squeeze-film air damping occurs when a thin layer of air is trapped between two closely spaced surfaces, such as a movable and a fixed electrode. As the movable surface oscillates or moves, the air in between is compressed and squeezed out, creating resistance and reducing the motion. On the other hand, slide-film air damping arises when the proof mass moves parallel to a structure surface, causing the air to slide between them and generate drag. Both mechanisms influence the dynamic behavior of MEMS devices. Understanding these damping effects is crucial for optimizing the design and functionality of MEMS sensors and actuators. Thus, one-axis differential capacitive MEMS accelerometer with ability of tuning post-fabrication resonance frequency, enhancing sensitivity, and having simple structure for fabrication compared with previously reported similar ones is necessary to develop. Moreover, a theoretical model for optimizing the sensor's design and investigating its operation characteristics including frequency response and damping is still lacking in sensor models reported in the literature.

In this article, we present a new model of one-axis MEMS acceleration sensor using a differential capacitive sensing mechanism with enhanced sensitivity. The sensor with a model features two masses which are separated from a single mass. The electrostatic tuning method is employed to compensate for the frequency mismatch in the case of two masses, ensuring that the resonance frequency of the sensor is the same as that of the sensor with a single mass. In addition to compensating for frequency mismatch, the tuning method also serves another crucial purpose that is to enhance the sensitivity of the sensor and post-fabrication tuning.

The remainder of the paper is structured as follows: Section 2 describes models of a one-axis MEMS accelerometer with a single mass and dual mass. The numerical results are presented in Section 3. Section 4 summarizes some main results and new contributions of the article.

2. Models of one-axis MEMS accelerometer

2.1. Model of one-axis MEMS accelerometer with a single mass

Fig. 1a shows a model of a one-axis accelerometer, consisting of a proof mass M suspended by a system of four folded springs. Fig. 1b shows the detail dimensions of a single folded spring (K_{1S}). At both ends of the proof mass, comb finger electrodes are attached to convert oscillations into sensing capacitance. Table 1 and Table 2 present the dimension parameters of M, sensing comb fingers, and K_{1S}.

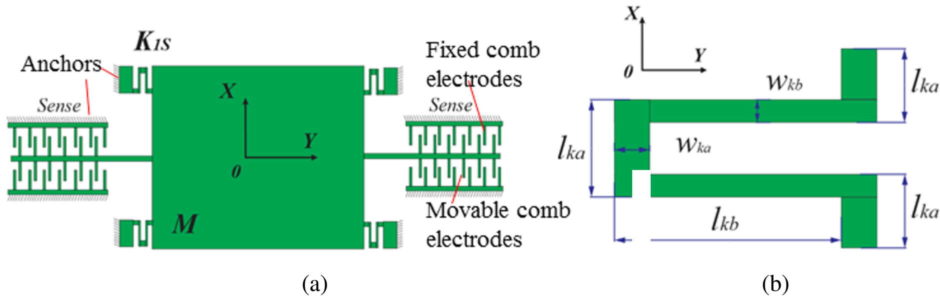

Fig. 1. a) The sensor model with a single proof mass M and b) Dimensions of a single folded spring (K_1S)

Table 1. Parameters of one-axis MEMS accelerometer with the single proof mass, and the double mass

Components	Parameters	Symbol	Values
Proof mass M	Length × Width × Height	$L \times W \times H$	3178 μm × 3178 μm × 20 μm
Frame M_1	Length × Width × Height	$L_1 \times W_1 \times H_1$	3290 μm× 3290 μm × 20 μm
Proof mass M_2	Length × Width × Height	$L_2 \times W_2 \times H_2$	920 μm × 525 μm × 20 μm
Sensing comb fingers	Length × Width × Gap distance × Finger number	$L_s \times B \times d_0 \times N_s$	100 μm × 10 μm × 1.5 μm × 400

Table 2. Dimensions of a single folded spring K_{1S}

Parameters	Symbol	Values
Thickness of the folded-spring	h	20 μm
Length of one beam	l_{kb}	89 μm
Width of one beam	w_{kb}	15 μm
Width of connection beam	w_{ka}	18 μm
Length of connection beam	l_{ka}	35 μm
Spring constant of four-fold spring	K_1	16246 N/m

The spring constant of the system with the four folded springs along the X–axis (Fig. 1b) is calculated by [27]:

$$K_1 = \frac{48EI_{z,b}[3\tilde{l}_{ka} + 2l_{kb}]}{2l_{kb}^2(12\tilde{l}_{ka}^2 + 12\tilde{l}_{ka}l_{kb} + 2l_{kb}^2)}. \tag{1}$$

Here, $I_{z,a} = hw_{ka}^3/12$ is the inertia moment of beam with length l_{ka}, $I_{z,b} = hw_{kb}^3/12$ is the inertia moment of beam with length l_{kb}, and $\tilde{l}_{ka} = I_{z,b})l_{ka}/I_{z,a}$. The Young's modulus ($E$) and density ($\rho$) of silicon are 168.9 GPa and 2330 Kg/m^3, respectively.

The motion equation of the sensor is modeled by a damped, harmonic oscillator as follows [28]:

$$m\ddot{x} + C_{\text{total}}\dot{x} + K_1 \times = ma\sin(\omega t). \tag{2}$$

Here, x, $\dot{x}$, and $\ddot{x}$ are the displacement, velocity, and acceleration of M relative to the ground, respectively, m is the proof mass's weight, C_{total} is damping coefficient of the proof mass M, and $a\sin(\omega t)$ is acceleration acting on the proof mass. By solving Eq. (2), the oscillation amplitude of $M(X)$ is obtained by

$$X = \frac{ma}{K_1\sqrt{\left(2\zeta\frac{\omega}{\omega_0}\right)^2 + \left(1-\left(\frac{\omega}{\omega_0}\right)^2\right)^2}}, \tag{3}$$

in which, ζ is damping ratio and is calculated according to the formula $\zeta = C_{\text{total}}/(2m\omega_0)$, and ω_0 is the resonant angular frequency of the system calculated by the formula $\omega_0 = \sqrt{K_1/m}$.

For calculations regarding capacitance, when there is a displacement x caused by an acceleration acting on the proof mass, the initial capacitance of the sensing comb electrodes on the decreasing (C_{1X}) and increasing (C_{2X}) side changes as [29]:

$$C_{1X} = \frac{N_s \varepsilon L_s B}{d_0 + x} \quad \text{and} \quad C_{2X} = \frac{N_s \varepsilon L_s B}{d_0 - x}. \tag{4}$$

Therefore, the differential capacitance change ΔC is derived as follows

$$\Delta C = C_{1X} - C_{2X} = \frac{2\varepsilon L_s B N_s x}{d_0^2 - x^2}. \tag{5}$$

2.2. Model of one-axis MEMS accelerometer having a frame and a proof mass without tuning resonant frequency

In this case, we divide the proof mass M (Fig. 1a) into the frame M_1 and the proof mass M_2 as shown in Fig. 2a. M_2 is connected to M_1 through a system of four folded springs (K_{1S}), while M_1 is connected to the base through four folded springs (K_{2S}). The dimension parameters of M_1, M_2, and K_{2S} are presented in Table 1 and Table 3. Compared with the model in Fig. 1a, the sensor model in Fig. 2a has a clear distinction with a separate mass and a frame. Fig. 2b illustrates the oscillation model of the accelerometer with an input acceleration of $a\sin(\omega t)$. C_1 is the damping coefficient of M_1 relative to the base, C_3 is the damping coefficient of M_2 relative to the base, while C_2 is the damping coefficient of M_2 relative to M_1.

The system of dual oscillation equations is expressed as [30]:

$$\begin{aligned} m_1\ddot{x}_1 + C_1\dot{x}_1 + K_1x_1 + C_2(\dot{x}_1 - \dot{x}_2) + K_2(x_1 - x_2) &= m_1 a\sin(\omega t) \\ m_2\ddot{x}_2 + C_3\dot{x}_2 + C_2(\dot{x}_2 - \dot{x}_1) + K_2(x_2 - x_1) &= m_2 a\sin(\omega t) \end{aligned} \tag{6}$$

x_1, $\dot{x}_1$, and $\ddot{x}_1$ are the displacement, velocity, and acceleration of M_1 relative to the ground, respectively, while x_2, $\dot{x}_2$, and $\ddot{x}_2$ are the displacement, velocity, and acceleration of M_2 relative to the ground, respectively.

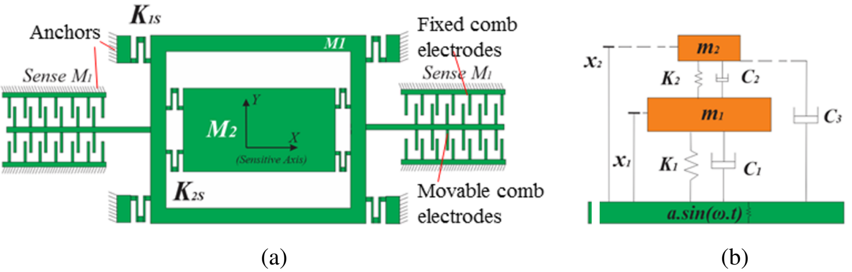

Fig. 2. a) Sensor model with the frame M_1 and the proof mass M_2 and b) Oscillation model of the sensor without tuning resonant frequency

Table 3. Dimensions of a single folded spring K_{2S}

Parameters	Symbol	Values
Thickness of the folded spring	h	10 μm
Length of one beam	l_{kb}	95 μm
Width of one beam	w_{kb}	5 μm
Width of connection beam	w_{ka}	10 μm
Length of connection beam	l_{ka}	40 μm
Spring constant of four-fold spring	K_2	398 N/m

We set

$$\omega_1^2 = \frac{K_1}{m_1}; \quad \omega_2^2 = \frac{K_2}{m_2}; \quad r = \frac{m_2}{m_1}; \quad \zeta_1 = \frac{C_1}{2m_1\omega_1}; \quad \zeta_2 = \frac{C_3}{2m_2\omega_2}$$
$$C_2 = n_3 C_3; \quad C_2 = n_1 C_1; \quad p = \frac{\omega_2}{\omega_1}; \quad \text{and} \quad g = \frac{\omega}{\omega_1}. \tag{7}$$

Here, ω_1 and ω_2 are the natural angular frequencies of M_1 and M_2, respectively, K_1 is the spring constant of the system consisting of four K_{1S} springs, while K_2 is the spring constant of the system consisting of four K_{2S} springs (Fig. 2a), r is the mass ratio between m_2 and m_1. ζ_1 and ζ_2 are the damping ratios of M_1 and M_2 (relative to the base). n_3 is defined as the ratio between the damping coefficients C_2 and C_3, and n_1 is defined as the ratio between the damping coefficients C_2 and C_1.

The oscillation amplitude of $M_1(X_1)$ is calculated as:

$$X_1 = \frac{am_1}{K_1}\sqrt{\frac{A}{B}}. \tag{8}$$

In Eq. (8), A and B are calculated by the following expressions:

$$A = [(p^2 - g^2) + rp^2]^2 + g^2[(n_3+1)2\zeta_2 p + n_1 2\zeta_1]^2, \tag{9}$$

$$B = [(1-g^2)(p^2-g^2) - (n_3+1)2\zeta_1 2\zeta_2 p g^2 - r g^2 p^2 - n_1 2\zeta_1 2\zeta_2 p g^2]^2 + g^2[2\zeta_1(p^2-g^2) + (n_3+1)2\zeta_2 p(1-g^2) + r 2\zeta_2 p^3 - n_1 g^2 2\zeta_1]^2. \tag{10}$$

The oscillation amplitude of $M_2(X_2)$ is calculated as

$$X_2 = \frac{am_1}{K_1}\sqrt{\frac{C}{D}}. \tag{11}$$

In Eq. (11), C and D are calculated by the following expressions:

$$\begin{aligned} C =& \{(1-g^2)(p^2-g^2) - (n_3+1)2\zeta_1 2\zeta_2 pg^2 - rg^2p^2 - n_1 2\zeta_1 2\zeta_2 pg^2 \\ &+ p^2[(p^2-g^2)+rp^2] - n_3 2p\zeta_2 gg[(n_3+1)2\zeta_2 p + n_1 2\zeta_1]\}^2 \\ &+ g\{2\zeta_1(p^2-g^2) + (n_3+1)2\zeta_2 p(1-g^2) + r2\zeta_2 p^3 - n_1 g^2 2\zeta_1 \\ &+ [(n_3+1)2\zeta_2 p + n_1 2\zeta_1]p^2 + n_3 2p\zeta_2[(p^2-g^2)+rp^2]\}^2, \end{aligned} \tag{12}$$

$$\begin{aligned} D =& \{[(1-g^2)(p^2-g^2) - (n_3+1)2\zeta_1 2\zeta_2 pg^2 - rg^2p^2 \\ &- n_1 2\zeta_1 2\zeta_2 pg^2](p^2-g^2 - g[2\zeta_1(p^2-g^2) + (n_3+1)2\zeta_2 p(1-g^2) \\ &+ r2\zeta_2 p^3 - n_1 g^2 2\zeta_1]2\zeta_2 pg(n_3+1)\}^2 + +g^2\{2\zeta_2 p(n_3+1)[(1-g^2)(p^2-g^2) \\ &- (n_3+1)2\zeta_1 2\zeta_2 pg^2 - rg^2p^2 - n_1 2\zeta_1 2\zeta_2 pg^2][2\zeta_1(p^2-g^2) \\ &+ (n_3+1)2\zeta_2 p(1-g^2) + r2\zeta_2 p^3 - n_1 g^2 2\zeta_1][p^2-g^2]\}^2. \end{aligned} \tag{13}$$

2.3. Model of one-axis MEMS accelerometer having a frame and a proof mass with enhanced sensitivity based on tuning resonant frequency

2.3.1. Concept of tuning sensor sensitivity

To tune the resonant frequency of M_1, we propose a sensor model having a frame M_1 and a proof mass M_2 similar to Fig. 2a with two electrostatic comb-drive microactuators using the tuning voltages, V_{t1} and V_{t2} as shown in Fig. 3. In this study, we have added the two laterally-driven electrostatic microactuators to tune the resonant frequency of M_1 and/or M_2. M_1 is considered as an inertial proof mass integrated the sensing comb electrodes for detecting external acceleration, while M_2 is a resonator integrated on M_1. However, our proposed structure is different from Ref. [14], in which one used the two electrostatically-driven torsional resonators integrated on an inertial proof mass to control the accelerometer's sensitivity. Moreover, using the two torsional resonators to form a differential measure of frequency variation is quite complicated, which limits its practical application. Now, we consider the displacement of M_1 or M_2. The equilibrium condition of the electrostatic force and the elastic force is defined by [27]:

$$F = F_e + F_k = 0, \tag{14}$$

where F_e represents the electrostatic force, and $F_k = -kx$ denotes the elastic restoring force. Here, k represents the stiffness of either K_1 or K_2. The equilibrium

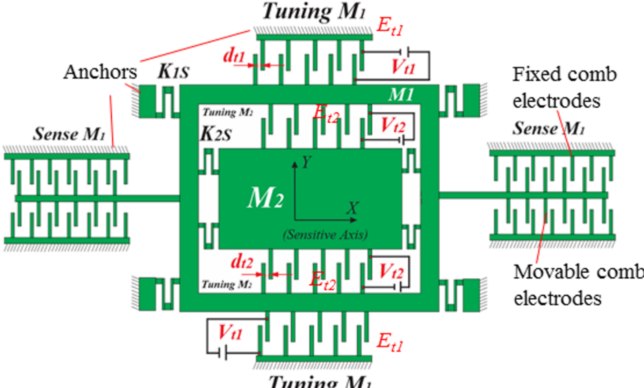

Fig. 3. Sensor model the same as Fig. 2a but with tuning comb electrodes E_{t1} and E_{t2}

displacement can be found from Eq. (14) by

$$\frac{A\varepsilon V^2}{2(d-x)^2} - kx = 0. \tag{15}$$

Here, ε represents the dielectric constant of air, and A denotes the area of the tuning comb electrode. V is the applied voltage for tuning the resonant frequency; if tuning the resonant frequency of M_1, the tuning comb electrodes E_{t1} are used, and if tuning the resonant frequency of M_2, the tuning comb electrodes E_{t2} are used. d is the gap distance between the tuning comb fingers, with d_{t1} for tuning the resonant frequency of M_1, and d_{t2} for tuning the resonant frequency of M_2. Considering the mathematical condition for stability, $\mathrm{d}F/\mathrm{d}x < 0$, we obtain

$$\frac{A\varepsilon V^2}{(d-x)^3} - k < 0. \tag{16}$$

From Eq. (16), we get

$$x < \frac{d}{3}. \tag{17}$$

This implies that the equilibrium displacement is stable when the proof mass's balanced position is less than one-third of its initial distance from the fixed electrode. This situation corresponds to applying a voltage that is smaller than $V_{\text{pull-in}}$. $V_{\text{pull-in}}$ is calculated by

$$V_{\text{pull-in}} = \sqrt{\frac{8}{27}\frac{kd^3}{A\varepsilon}}. \tag{18}$$

2.3.2. Model of one-axis MEMS accelerometer with tuned resonant frequency

Based on the equation system (6), the amplitudes of M_1 and M_2 with tuned resonant frequency are described as:

$$m_1\ddot{x}_1 + C_1\dot{x}_1 + K_1x_1 + C_2(\dot{x}_1 - \dot{x}_2) + K_2(x_1 - x_2) - F_{1\text{electric}} = m_1 a\sin(\omega t), \tag{19}$$

$$m_2\ddot{x}_2 + C_3\dot{x}_2 + C_2(\dot{x}_2 - \dot{x}_1) + K_2(x_2 - x_1) - F_{2\text{electric}} = m_2 a \sin(\omega t). \tag{20}$$

In Eqs. (19) and (20), $F_{1\text{electric}}$ and $F_{2\text{electric}}$ are the electrostatic forces generated by the two comb capacitors in the x direction acting on M_1 and M_2 (Fig. 3), respectively.

Let x_{it} be the initial displacement of the frame or mass M_i caused by tuning K_i $(i = 1, 2)$, we have

$$K_i - \frac{\varepsilon l_{ti} w_{ti} N_{ti} V_i^2}{(d_{ti} - x_{it})^3} = K_i', \tag{21}$$

$$(d_{ti} - x_{it})^3 = \frac{\varepsilon l_{ti} w_{ti} N_{ti} V_i^2}{K_i - K_i'}. \tag{22}$$

Here, K_i' is the i-th spring constant after tuning, which relates to the spring softening effect caused by electrostatic force [21, 22].

Parameters for tuningK_1 and K_2 are shown in Table 4.

Table 4. Parameters for tuning K_1 and K_2

Parameters	K_1	Values for K_1	K_2	Values for K_2
Comb finger length	l_{t1}	100 µm	l_{t2}	100 µm
Comb finger width	w_{t1}	20 µm	w_{t2}	20 µm
Gap distance between tuning comb fingers	d_{t1}	3 µm	d_{t2}	3 µm
Number of movable tuning comb fingers	N_{t1}	200	N_{t2}	100
Applied tuning voltage	V_{t1}	98.65 (V)	V_{t2}	22.21 (V)
Pull-in voltage	$V_{t1_{\text{pull-in}}}$	191.5 (V)	$V_{t2_{\text{pull-in}}}$	44.2 (V)
Spring constant before tuning	K_1	16246 N/m	K_2	398 N/m
Spring constant after tuning	K_1'	14790 N/m	K_2'	360.9 N/m

Setting $\tilde{x}_{it} = \dfrac{x_{it}}{d_{ti}}$, we have

$$(1 - \tilde{x}_{it})^3 = \frac{\varepsilon l_{ti} w_{ti} N_{ti} V_i^2 / d_{ti}^3}{K_i - K_i'}. \tag{23}$$

At the equilibrium position, we have the equation

$$\frac{\varepsilon l_{ti} w_{ti} N_{ti} V_i^2}{2(d_{ti} - x_{it})^2} - K_i x_{it} = 0. \tag{24}$$

Eq. (24) is equivalent to

$$\tilde{x}_{it}(1 - \tilde{x}_{it})^2 = \frac{\varepsilon l_{ti} w_{ti} N_{ti} V_i^2 / 2d_{ti}^3}{K_i}. \tag{25}$$

Dividing both sides of equations (23) and (25), we get:

$$x_{it} = \frac{K_i - K_i'}{3K_i - K_i'} d_{ti}. \tag{26}$$

From Eqs. (24) and (26), we have:

$$x_{it} = \frac{K_i - K_i'}{3K_i - K_i'} d_{ti}, \tag{27}$$

$$V_i = \sqrt{\left(\frac{2K_i}{3K_i - K_i'}\right)^3 \frac{(K_i - K_i')d_{ti}^3}{\varepsilon l_{ti} w_{ti} N_{ti}}}. \tag{28}$$

Pull-in voltage for tuning the stiffness K_i:

$$V_{ti_{\text{pull-in}}} = \sqrt{\frac{8}{27} \frac{K_i d_{ti}^3}{\varepsilon l_{ti} w_{ti} N_{ti}}}. \tag{29}$$

From there, we can deduce the values of the initial displacements:

$$X_{01} = x_{1t} + \frac{K_2 x_{2t}}{K_1'}), \tag{30}$$

$$X_{02} = x_{2t} + x_{1t} + \frac{K_2 x_{2t}}{K_1'}. \tag{31}$$

The oscillation equations at the new equilibrium position after tuning are described by

$$m_1\ddot{x}_1 + C_1\dot{x}_1 + K_1'x_1 + C_2(\dot{x}_1 - \dot{x}_2) + K_2'(x_1 - x_2) = m_1 a \sin(\omega t), \tag{32}$$

$$m_2\ddot{x}_2 + C_3\dot{x}_2 + C_2(\dot{x}_2 - \dot{x}_1) + K_2'(x_2 - x_1) = m_2 a \sin(\omega t). \tag{33}$$

The method for solving equations (32) and (33) is similar to that for solving the system of equations (6), as presented above. From solving the above system of equations, we obtain the oscillation amplitude of the frame M_1 as X_{1T} and the oscillation amplitude of the mass M_2 as X_{2T}.

2.4. Damping calculation in the sensor

The impact of damping on the behavior of the sensors is quite evident. Air damping consists of two main components: slide film air damping and squeeze-film air damping [23]. Each component influences the structure described as follows. In the case of slide film air damping, given that the gap distance(distance from the

mass to substrate), denoted as d_t, is significantly smaller than δ (δ is the effective decay distance), the damping coefficient takes the form of a Couette-flow type and can be represented as [23]:

$$c_{\text{cf}} = \mu \frac{A_q}{d_t}. \tag{34}$$

Here, A_q is the surface area of the proof mass or the frame. In the case where the moving structure of the sensor is situated far from any objects positioned above it, the damping force acting on the moving parts follows a Stokes-flow pattern. The corresponding damping coefficient is calculated by

$$c_{\text{sf}} = \mu \frac{A_q}{\delta}. \tag{35}$$

The assessment of the air drag force on the proof mass is complex. An approximation for its coefficient is given by

$$c_{\text{df}} = \frac{32}{3} \mu l. \tag{36}$$

Here, l represents the characteristic dimension of the moving structure, which may be considered as half the width of the proof mass. In the case of squeeze-film air damping, the coefficient of damping force for a rectangular comb finger is calculated by

$$C_{\text{squ}} = \frac{N_s \mu B^3 L_s}{d_0^3}. \tag{37}$$

The total damping coefficient is calculated by [23]:

$$C_{\text{total}} = c_{\text{cf}} + c_{\text{sf}} + c_{\text{df}} + C_{\text{squ}}, \tag{38}$$

$$C_{\text{total}} = \mu \frac{A_q}{d_t} + \mu \frac{A_q}{\delta} + \mu l \frac{32}{3} + \frac{N_s \mu B^3 L_s}{d_0^3}. \tag{39}$$

3. Results and discussion

3.1. Results of one-axis MEMS accelerometer having one proof mass

3.1.1. Damping coefficient of the sensor with one proof mass

At the sensing comb finger gaps $d_0 = 0.5$µm, 1 µm, and 1.5 µm, the total damping coefficients of the sensor calculated according to Eq. (39) are $C_{\text{total}} = 5.88\times10^{-3}$ Ns/m, 8.37×10^{-4} Ns/m, and 3.31×10^{-4} Ns/m, respectively. Therefore, the damping ratios of the sensor according to Eq. (7)are $\zeta = \dfrac{C_{\text{total}}}{2M\pi\omega_0} = \dfrac{C_{\text{total}}}{2\sqrt{MK_1}} =$

0.0336, 0.0048, and 0.0019, respectively. Moreover, the quality factor of the sensor is calculated by $Q = 1/(2\zeta)$. Therefore, the Q value at the corresponding sensing comb finger gaps are 14, 104, and 263. The resonance frequency (f_s) of the sensor is calculated by $f_s = \frac{1}{2\pi}\sqrt{\frac{K_1}{m}} = 29.592$ kHz. This resonance frequency is suitable for sensor applications in vibration measurements [1].

Fig. 4 shows the relationship between the oscillation amplitude of M investigated as a function of the input acceleration frequency with different values of the total damping coefficient according to the different sensing comb finger gaps above. Thus, the larger the damping coefficient, the smaller the oscillation amplitude is. Observing Fig. 4, we can see that the amplitude of M reaches 7.4 nm at $d_0 = 1.5$ µm, which is larger than 17.7 times that at $d_0 = 0.5$ µm at the same resonant frequency of 29.592 kHz.

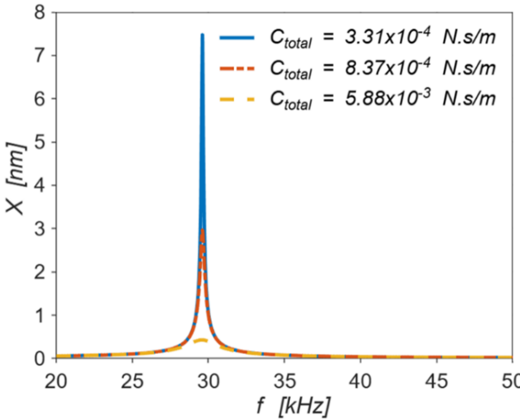

Fig. 4. Oscillation amplitude of the sensor with the single proof mass M depending on frequency for different total damping coefficients

3.1.2. Sensitivity of the sensor with one proof mass

Fig. 5 presents the dependence of ΔC on the input acceleration, a, for the three different values of d_0, $d_0 = 0.5$ µm, 1 µm, and 1.5 µm. Thus, the sensing capacitance depends linearly on a. When $a = 0.1$ g, ΔC is approximately 0.0239 pF with $d_0 = 1.5$ µm. The value of ΔC is relatively small and challenging to measurements. So, the posed question is how to increase sensitivity while still maintaining the resonance frequency (at $f_s = 29.592$ kHz). Therefore, we have proposed a new model of the sensor structure for enhancing the sensing capacitance. We has separated the proof mass M into the frame M_1 and the proof mass M_2, as illustrated in Fig. 2. In the following sections, we will present the obtained results from the proposed novel sensor model.

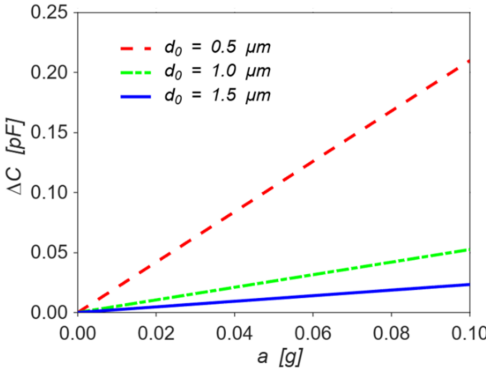

Fig. 5. Differential capacitance investigated as a function of a for three different values of d_0, d_0 = 0.5 µm, 1 µm, and 1.5 µm

3.2. Results of one-axis MEMS accelerometer having one proof mass split into a frame and a proof mass

3.2.1. Without tuning resonant frequency

The damping coefficient of M_1 before tuning is calculated in the same way as that of the sensor with a proof mass M in Section 3.1. At $d_0 = 1.5$µm, the damping coefficient M_1 is calculated according to Eq. (39) to be $C_1 = 3.25 \cdot 10^{-4}$ Ns/m. Therefore, damping ratio $\zeta_1 \left(= \dfrac{C_1}{2\sqrt{m_1 K_1}} \right)$ is 0.00188 and Q_1 is 266.

Fig. 6 presents C_3 of M_2 before tuning investigated as a function of A_{q2} for three different distances between the moving structures of the sensor and the substrate. At $A_{q2} = 483000$ µm^2, C_3 is $6 \cdot 10^{-6}$ Ns/m. Therefore, the damping ratio

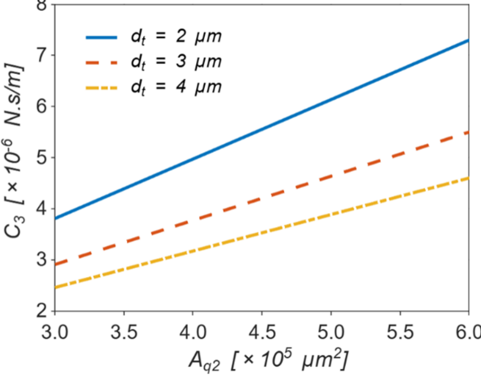

Fig. 6. C_3 of the mass M_2 before tuning investigated as a function of A_{q2} for three different distances between the moving structures of the sensor and the substrate

is $\zeta_2 \left(= \dfrac{1}{2Q_2} = \dfrac{C_3}{2\sqrt{m_2 K_2}}\right) = 0.001$. In this case, the quality factor of the sensor is obtained to be 500.

Fig. 7 presents the dependence of X_1 investigated as a function of the input acceleration frequency for the ratios $\omega_2/\omega_1 = [1.0, 1.1, 1.2, 1.4, 1.7, 2, 3, 6, 8, 10]$. Thus, when ω_2/ω_1 increases from 1.0 to 1.7, X_1 tends to increase steadily. Meanwhile, ω_2/ω_1 increases sequentially from 1.7 to 10, X_1 tends to decrease. Interestingly, as ω_2/ω_1 increases, the resonant frequency (f_{M1}) of the frame M_1 is lower than the resonant frequency in the single mass case.

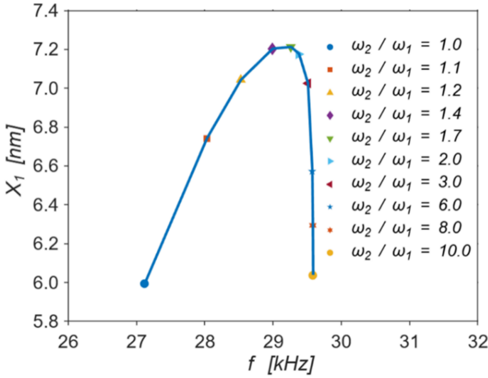

Fig. 7. X_1 of M_1 investigated as a function of the frequency of the input acceleration for the ratios $\omega_2/\omega_1 = [1.0, 1.1, 1.2, 1.4, 1.7, 2, 3, 6, 8, 10]$

Fig. 8 shows the relationship between X_1 and the input acceleration frequency for different values of ω_2/ω_1 smaller than 1. From Fig. 8a, we can see that as ω_2/ω_1 increases sequentially from 0.01 to 0.1, X_1 tends to decrease slowly, and the resonant frequency for these values of X_1 tends to remain unchanged, approaching the value $f_{M1} = 30.321$ kHz. From Fig. 8b, we can see that as ω_2/ω_1 increases sequentially from 0.1 to 0.9, X_1 also tends to decrease sharply, and the resonant frequency for these values ofX_1 tends to increase. This increase in the resonant frequency is more pronounced compared to the case shown in Fig. 8a. At the position where $\omega_2/\omega_1 = 0.7$, X_1 is 6.55 nm and the resonance frequency is 31.02 kHz.

Fig. 9 presents X_1 of M_1 investigated as a function of the frequency of the input acceleration for the two ranges of the ratio m_2/m_1: $m_2/m_1 < 1$ and $m_2/m_1 > 1$, respectively. When m_2/m_1 decreases from 0.8 to 0.01, X_1 increases, and the resonance frequency decreases (Fig. 9a). And when m_2/m_1 decreases further, the resonance frequency approaches a value of 30.394 kHz. With $m_2/m_1 = 0.05$, X_1 equals 6.55 nm, and the resonance frequency equals 31.02 kHz. In Fig. 9b, as m_2/m_1 increases from 1 to 2.5, X_1 increases gradually, while the resonance

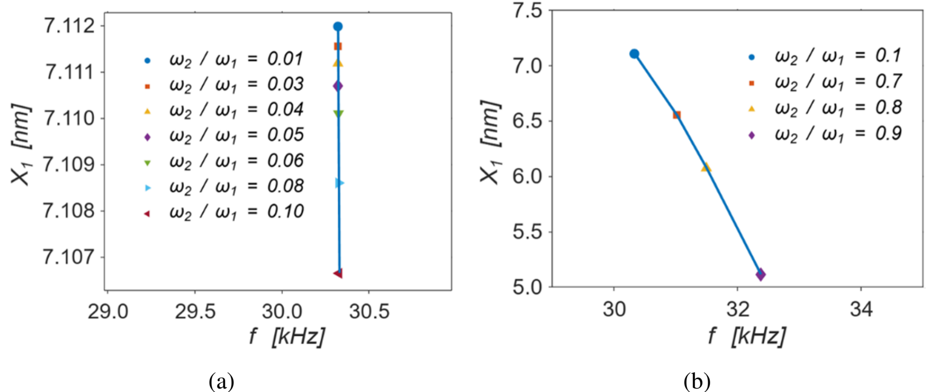

Fig. 8. X_1 of M_1 investigated as a function of the frequency of the input acceleration in the cases: a) with $\omega_2/\omega_1 = [0.01, 0.03, 0.04, 0.05, 0.06, 0.08, 0.1]$ and b) with $\omega_2/\omega_1 = [0.1, 0.7, 0.8, 0.9]$

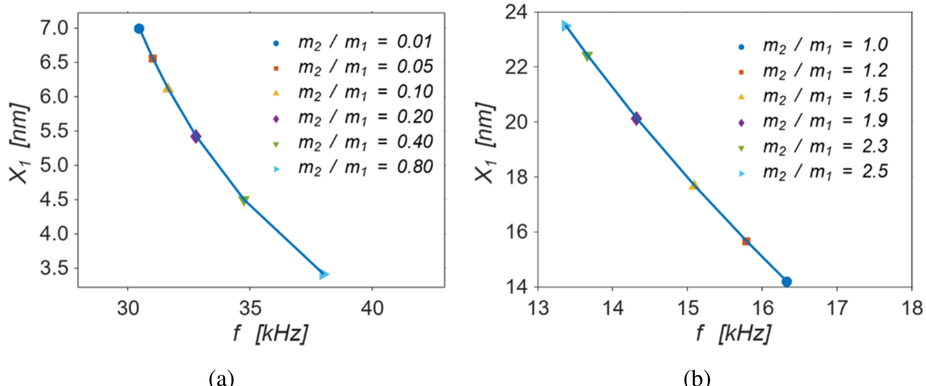

Fig. 9. X_1 of M_1 investigated as a function of the frequency of the input acceleration for: a) $m_2/m_1 < 1$ and b) $m_2/m_1 \geqslant 1$

frequency decreases from 16.326 kHz to 13.369 kHz. The resonance frequency in this case is much lower than the resonance frequency of the single mass.

Based on the calculated analyses above, it is advisable to choose $m_2/m_1 < 1$ and $\omega_2/\omega_1 < 1$ for the following reasons. If we choose $m_2/m_1 > 1$, from Fig. 9b we can see that the resonance frequency is very low (13.369 kHz in the double mass case with $m_2/m_1 = 1$ compared to $f_0 = 29.592$ kHz in the single mass case). Therefore, the frequency tuning technique cannot be applied in this case. If $\omega_2/\omega_1 > 1$, from Fig. 7, it can be seen that the resonance frequency is always lower compared to the single mass case. Therefore, the resonance frequency tuning in this case is not also feasible. From the results shown in Fig. 8b, we choose $\omega_2/\omega_1 = 0.7$, and based on Fig. 9a, we choose $m_2/m_1 = 0.05$ as the calculated results.

In Fig. 10a, when the spring stiffness K_1 is 16246 N/m, the maximum amplitude is achieved a value of 7.4 nm at the resonance frequency of 29.592 kHz. In Fig. 10b,

K_1 is varied with different values, K_1 = 16246 N/m, 14790 N/m, and 13000 N/m. When the spring stiffness is K_1 = 16246 N/m, the amplitude reaches its maximum value at the resonance frequency of 31.02 kHz. As the value of K_1 decreases, we observe a slight increase in the resonant amplitude due to the decrease of the resonance frequency. For example, when K_1 = 14790 N/m, the resonance frequency is 29.592 kHz, matching the resonance frequency of the single mass case. Therefore, the problem posed is to reduce the resonance frequency from 31.02 kHz to 29.592 kHz, which means reducing the spring stiffness K_1 from 16246 N/m to 14790 N/m.

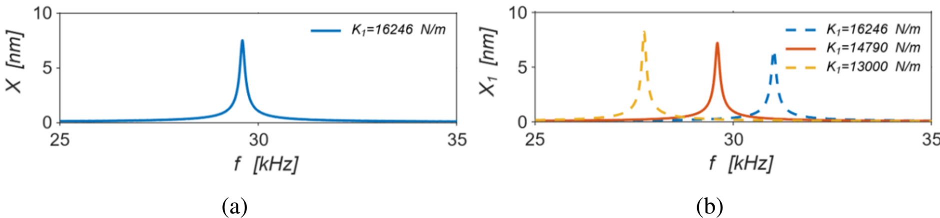

Fig. 10. a) X of the single mass investigated as a function of frequency, b) X_1 of the frame M_1 in the case of double mass investigated as a function of frequency with the different values of K_1

To address the problem, we will consider the tuning method for K_1. Advantages of the tuning method for K_1 are to reduce the stiffness of the spring while increasing the initial oscillation amplitude. However, there is an issue. When the stiffness of K_1 decreases, ω_2/ω_1 increases.

The results in Fig. 8b show that increasing the value of ω_2/ω_1 will increase the resonance frequency. Therefore, this reduces the effectiveness of tuning K_1. To achieve the desired effect of reducing the resonance frequency from 31.02 kHz to 29.592 kHz, for M_1, tuning is required for both K_1 and K_2 of M_2 to maintain ω_2/ω_1 constant. Thus, along with reducing K_1 from 16246 N/m to 14790 N/m, K_2 also decreases from 398 N/m to 360.9 N/m. Furthermore, when tuning the resonance frequency of both M_1 and M_2, the damping of both M_1 and M_2 also needs recalculated due to the additional air resistance from the tuning comb electrodes.

Fig. 11 presents C_2 of M_2 compared with M_1 investigated as a function of the number of movable tuning comb fingers (N_{t2}) for tuning K_2 for three tuning comb finger gaps. At d_0 = 1.5µm, C_1 is 4.38×10^{-4} Ns/m. Therefore, the damping ratio is $\zeta_1 = \dfrac{C_1}{2\sqrt{m_1 k_1}} = 0.0027$. From Fig. 11, the damping coefficient C_2 is calculated to be 5.33×10^{-5} Ns/m. Therefore, $n_1 = \dfrac{C_2}{C_1} = \dfrac{5.33 \cdot 10^{-5}}{3.25 \cdot 10^{-4}} = 0.164$ and $n_3 = \dfrac{C_2}{C_3} = \dfrac{5.33 \cdot 10^{-5}}{6 \cdot 10^{-6}} = 8.883$.

www.czasopisma.pan.pl PAN POLSKA AKADEMIA NAUK www.journals.pan.pl

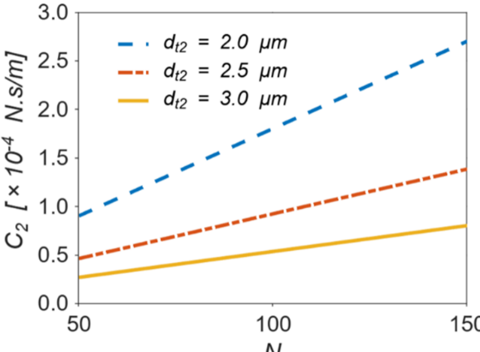

Fig. 11. C_2 of M_2 compared with M_1 investigated as a function of N_{t2} for three tuning comb finger gaps, d_{t2} = 2, 2.5, and 3 μm, respectively

3.2.2. Tuning K_1 and K_2

Fig. 12 shows variation of the spring stiffness versus applied voltage for the different tuning comb finger gaps. From Fig. 12a, we can see that as the tuning comb finger gap increases, $V_{t1_{\text{pull-in}}}$ (The value of V_{t1} when K_1 equals 0) also increases. For the case of $d_{t1} = 3\mu\text{m}$, $V_{t1_{\text{pull-in}}}$ calculated according to Eq. (29) is 191.5 V, and the applied voltage value calculated according to Eq. (28) is 98.65 V. In this case, we can decrease K_1 from 16246 N/m to 14790 N/m. Fig. 12b shows that as the tuning comb finger gap increases, $V_{t2_{\text{pull-in}}}$ (the value of V_{t2} when K_2 equals 0) also increases. For the case of $d_{t2} = 3\mu\text{m}$, $V_{t2_{\text{pull-in}}}$ calculated according to Eq. (29) is 42.4 V, and the applied voltage value calculated according to Eq. (28) is 22.21 V. In this case, we can decrease K_2 from 398 N/m to 360.9 N/m.

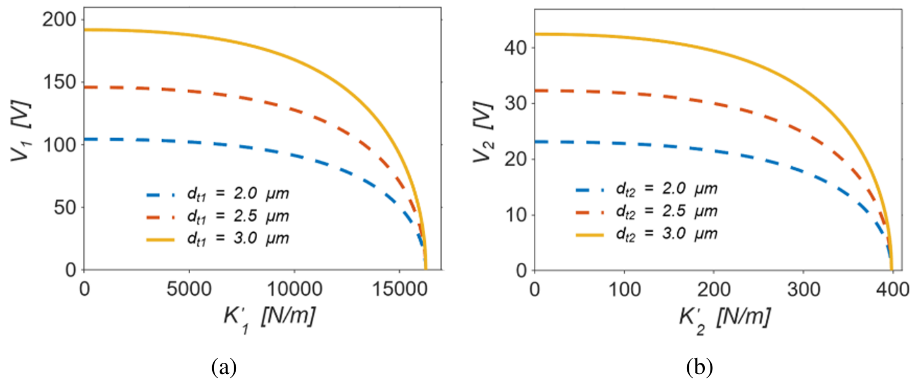

Fig. 12. Variation of the spring stiffness versus applied voltage for the different tuning comb finger gaps: a) K'_1 versus V_1 for d_{t1} = 2, 2.5, and 3 μm and b) K'_2 versus V_2 for d_{t2} = 2, 2.5, and 3 μm

3.2.3. Amplitude of M_1 after tuning compared with its amplitude before tuning

After tuning, the amplitude of M_1 has significantly increased (Fig. 13a). In this investigation, the applied voltages for tuning the resonant frequency of M_1 and M_2 are shown in Table 4. At the resonant frequency f_0 = 29.592 kHz, the oscillation amplitude of M_1 at $C_1 = 4.38 \cdot 10^{-4}$ (Ns/m) is X_{1T} = 131.2 nm. While the amplitude (before tuning as shown in Fig. 10b) with the dashed light blue line at the resonance frequency of 31.02 kHz is 6.55 nm.

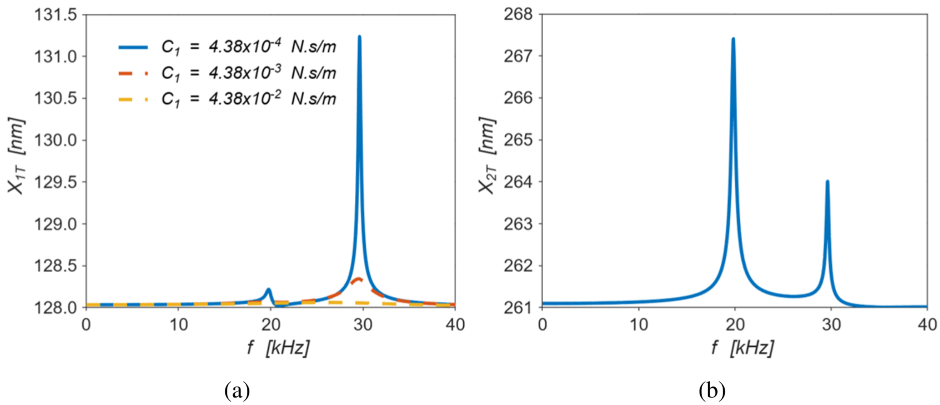

Fig. 13. a) Amplitude of M_1 in the double mass case after tuning b) Amplitude of M_2 after tuning

Table 5. Comparison of the oscillation amplitude and resonant frequency of the sensors having single proof mass and double mass before and after tuning

Parameters	Single mass	Double mass before tuning	Double mass after tuning
Amplitude of oscillation	7.4 nm	6.55 nm	131.2 nm
Resonant frequency	29.592 kHz	31.020 kHz	29.592 kHz

Because X_{1T} = 131.2 nm is smaller than $d_{t1}/3$ (= 1 µm), it helps to prevent the pull-in effect when tuning K_1. For a broader overview, the data illustrating the amplitude and resonant frequency of both the single mass and double mass sensors are presented in Table 5. From Table 5, the tuning process has successfully improved the sensing amplitude which is increased by a factor of 18 compared with that without tuning. In the tuning process, the resonance frequency is decreased by 4.5%. From Fig. 13b, at the resonance position of 29.592 kHz, X_2 reaches its maximum value at X_{2T} = 264 nm.

Thus, it is clear that under other unchanged conditions, the sensor's vibration amplitude with electrostatic tuning is always greater than that without tuning. When the initial distance between the tuning comb electrodes increases, K_i' increases (Eq. (21)), i.e., the resonant frequency increases), and the sensor's vibration amplitude decreases under other unchanged conditions. According to Eq. (5), the

www.czasopisma.pan.pl PAN POLSKA AKADEMIA NAUK www.journals.pan.pl

sensor's sensitivity is reduced. On the other hand, the increase of the gap between the sensing comb electrodes due to the reduced tuning amplitude leads to the decrease of damping (i.e., Q increases) in the sensor. Thus, a question is raised that what reason has made the sensor's vibration amplitude (the sensitivity increases) increase. This can be explained according to Ref. [31], the vibration amplitude of a resonator is proportional to Q and f_s^{-2}. Thus, the vibration amplitude of M_1 shows a stronger dependence on the resonant frequency than on Q. Moreover, the designed gap between the sensing comb electrodes is 1.5 μm, while the gap between the tuning comb electrodes is 3 μm, and the number of tuning comb electrodes is also smaller. Therefore, the influence of the tuning comb electrodes on damping is significantly lower than that of the sensing comb electrodes.

3.2.4. Sensitivity of the sensor in the case of double mass

Fig. 14 presents differential capacitance investigated as a function of input acceleration, a, for the three different values of the gap between the sensing comb fingers, d_0 = 0.5 μm, 1 μm, and 1.5 μm. The characteristics show a linear relationship between ΔC and a. When $a = 0.1g$, ΔC is approximately 0.425 pF with d_0 = 1.5 μm. After tuning, the achieved sensitivity value of the acceleration sensor in the double mass case is $\Delta C/g$ = 4.25 pF/g. Meanwhile, from Fig. 5, ΔC for the single mass case is 0.0239 pF with $a = 0.1g$ corresponding to the sensitivity is $\Delta C/g$ = 0.239 pF/g. Thus, the sensitivity of the double mass acceleration sensor after tuning is nearly 18 times greater than that of the single mass acceleration sensor. Moreover, compared with the achieved sensitivities in Refs. [32, 33] (around 0.2 pF/g), the proposed one-axis MEMS-accelerometer sensor has showed a superior sensitivity.

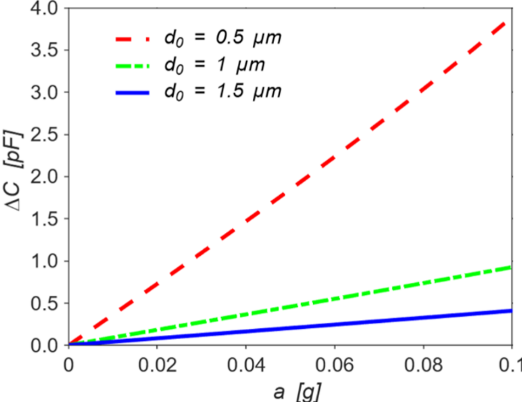

Fig. 14. Differential capacitance investigated as a function of the input acceleration, a, for the three different values of the gap between the sensing comb fingers, d_0 = 0.5 μm, 1 μm, and 1.5 μm

4. Conclusion

In summary, we have presented a single-axis, differential capacitive MEMS acceleration sensor with enhanced sensitivity based on a novel structure design and resonant frequency tuning method. The sensor consists of a proof mass symmetrically suspended at the center of a frame by folded springs. By applying electrostatic tuning method using comb electrodes integrated on both the proof mass and the frame, we can shift the initial resonance frequency of the sensor of 4.5%. Using the proposed tuning method, the resonance amplitude of sensor has been significantly improved. The sensitivity ($\Delta C/g$) of the sensor is enhanced by a factor of 18 compared to that of the single mass sensor. To ensure further the accuracy and reliability of the proposed sensor model, verification by experiment data and numerical simulation needs carried out in the future. This research provides an essential basis for the calculation and development of single-axis acceleration sensors for applications in mechanical oscillation measurements.

References

[1] N. Yazdi, F. Ayazi, and K. Najafi. Micromachined inertial sensors. *Proceedings of the IEEE*, 86(8):1640–1659, 1998. doi: 10.1109/5.704269.

[2] H. Kaplan, H. Bilgin, S. Yilmaz, H. Binici, and A. Öztas. Structural damages of L'Aquila (Italy) earthquake.*Natural Hazards and Earth System Sciences*, 10(3):499–507, 2010. doi: 10.5194/nhess-10-499-2010.

[3] M. Preeti, K. Guha, K.L. Baishnab, K. Dusarlapudi, and K.N. Raju. Low frequency MEMS accelerometers in health monitoring – A review based on material and design aspects. *Materials Today: Proceedings*, 18:2152–2157, 2019. doi: 10.1016/j.matpr.2019.06.658.

[4] D.W. Burns, R.D. Horning, W.R. Herb, J.D. Zook, and H. Guckel. Resonant microbeam accelerometers. In *Proceedings of the 8th International Conference on Solid-State Sensors and Actuators (Transducers'95)*, pages 659–662, Stockholm, Sweden, 25-28 June 1995. doi: 10.1109/SENSOR.1995.721918.

[5] K. Rao, H. Liu, X. Wei, W. Wu, C. Hu, J. Fan,J. Liu, and L. Tu. A high-resolution area-change-based capacitive MEMS tilt sensor. *Procedia Engineering*, 313:112191, 2020. doi: 10.1016/j.sna.2020.112191.

[6] R. Li, Z. Mohammed, M. Rasras, I.M. Elfadel, and D. Choi. Design, modelling and characterization of comb drive MEMS gap-changeable differential capacitive accelerometer. *Measurement*, 169:108377, 2021. doi: 10.1016/j.measurement.2020.108377.

[7] R. Mukhiya, M. Garg, P. Gaikwad, S. Sinha, A.K. Singh, and R. Gopal. Electrical equivalent modeling of MEMS differential capacitive accelerometer. *Microelectronics Journal*, 99:104770, 2020. doi: 10.1016/j.mejo.2020.104770.

[8] M. Keshavarzi and J.Y. Hasani. Design and optimization of fully differential capacitive MEMS accelerometer based on surface micromachining. *Microsystem Technologies*, 25:1369–1377, 2019. doi: 10.1007/s00542-018-4187-5.

[9] X. Gong, Y.C. Kuo, G. Zhou, W.J. Wu, and W.H. Liao. An aerosol deposition based MEMS piezoelectric accelerometer for low noise measurement. *Microsystems & Nanoengineering*, 9:23, 2023. doi: 10.1038/s41378-023-00484-5.

[10] C. Ge and E. Cretu. A polymeric piezoelectric MEMS accelerometer with high sensitivity, low noise density, and an innovative manufacturing approach. *Microsystems & Nanoengineering*, 9:151, 2023. doi: 10.1038/s41378-023-00628-7.

[11] C. Li, R. Zhang, L. Hao, and Y. Zhao. Development of a MEMS piezoresistive high-g accelerometer with a cross-center block structure and reliable electrode. *Sensors*, 24(17):5540, 2024. doi: 10.3390/s24175540.

[12] A. Meo, F. Garescì, V. Lopez-Dominguez, D. Rodrigues, E. Raimondo, V. Puliafito, P.K. Amiri, M. Carpentieri, and G. Finocchio. Magnetomechanical accelerometer based on magnetic tunnel junctions. *Physical Review Applied*, 20(3):034003, 2023. doi: 10.1103/PhysRevApplied.20.034003.

[13] M. Mahissi, W. Cai, X. Zhang, X. Tong, C. Zhang, X. Ma, and M. Dossou. Diaphragms simulation, fabrication, and testing of a high temperature fiber optic F-P accelerometer based on MEMS. *Optics Express*, 31(15):25025–25041, 2023. doi: 10.1364/oe.497730.

[14] C. Comi, A. Corigliano, A. Ghisi, and S. Zerbini. A resonant micro accelerometer based on electrostatic stiffness variation. *Meccanica*, 48:1893–1900, 2013. doi: 10.1007/s11012-013-9768-x.

[15] A. Mustafazade, M. Pandit, C. Zhao, G. Sobreviela,Z. Du, P. Steinmann, X. Zou, R.T. Howe, and A. Seshia. A vibrating beam MEMS accelerometer for gravity and seismic measurements. *Scientific Reports*, 10:10415, 2020. doi: 10.1038/s41598-020-67046-x.

[16] Y. Zhao, J. Zhao, X. Wang, G.M. Xia, A.P. Qiu, Y. Su, and Y.P. Xu. A sub-µg bias-instability MEMS oscillating accelerometer with an ultra-low-noise read-out circuit in CMOS. *IEEE Journal of Solid-State Circuits*, 50(9):2113–2126, 2015. doi: 10.1109/JSSC.2015.2431076.

[17] C. Zhao, M. Pandit, G. Sobreviela, P. Steinmann, A. Mustafazade, X. Zou, and A. Seshia. A resonant MEMS accelerometer with 56 ng bias stability and 98 ng/Hz$^{1/2}$ noise floor. *Journal of Microelectromechanical Systems*, 28(3):324–326, 2019. doi: 10.1109/JMEMS.2019.2908931.

[18] H. Ding, W. Wang, B.F. Jug, and J. Xin. A MEMS resonant accelerometer with sensitivity enhancement and adjustment mechanisms. *Journal of Micromechanics and Microengineering*, 27:115010, 2017. doi: 10.1088/1361-6439/aa8d99.

[19] X. Zou and A.A. Sasha. A high-resolution resonant MEMS accelerometer. In Proceedings of the 18th International Conference on Solid-State Sensors, Actuators and Microsystems (Transducers), pages 1247–1250, Anchorage, USA, 2015. doi: 10.1109/TRANSDUCERS.2015.7181156.

[20] Y. Zhang, S. Wang, Q. Yang, Y. Qi, M. Zhao, and X. Wei. A novel design of a MEMS resonant accelerometer with adjustable sensitivity. *Sensors and Actuators A: Physical*, 379:115859, 2024. doi: 10.1016/j.sna.2024.115859.

[21] K. Kawakami, S. Kaneuchi, H. Tanigawa, and K. Suzuki. MEMS resonator with wide frequency tuning range and linear response to control voltages for use in voltage control oscillators. *Journal of Micromechanics and Microengineering*, 29(12):125007, 2019. doi: 10.1088/1361-6439/ab4830.

[22] W. Zhang and J.E.Y. Lee. Frequency tuning in a MEMS resonator via an integral crossbar heater.*Procedia Engineering*, 47(3):949–952, 2012. doi: 10.1016/j.proeng.2012.09.303.

[23] M. Bao. *Analysis and Design Principles of MEMS Devices*, Elsevier, 2005.doi: 10.1016/B978-0-444-51616-9.X5000-0.

[24] A.A. Trusov, A.R. Schofield, and A.M. Shkel. Micromachined rate gyroscope architecture with ultra-high quality factor and improved mode ordering. *Sensors and Actuators A: Physical*, 165(1):26–34, 2011. doi: 10.1016/j.sna.2010.01.007.

[25] Y. Mo, H. Zhou, G. Xie, and B. Tang. Investigation of air damping effect in two kinds of capacitive MEMS accelerometers. *Microsystem Technologies*, 24(4):2017–2023, 2017. doi: 10.1007/s00542-017-3598-z.

[26] M.N. Nguyen, N.S. Ha, L.Q. Nguyen, H.M. Chu, and H.N. Vu. Z-axis micromachined tuning fork gyroscope with low air damping. *Micromachines*, 8(2):42, 2017. doi: 10.3390/mi8020042.

www.czasopisma.pan.pl PAN POLSKA AKADEMIA NAUK www.journals.pan.pl

[27] K. F. Gary. *Simulation of Microelectromechanical Systems*. PhD Thesis, Department of Electrical Engineering and Computer Sciences, University of California, USA, 1994.

[28] K. Terada, M. Karwa, N. Kumar, and R. Mohammed. Design and simulation of MEMS based capacitive accelerometers for crash detection and airbag deployment in automobile. *International Journal of Engineering Research & Technology (IJERT)*, 10(8):100–121, 2021.

[29] M. Benmessaoud and M. Nasreddine. Optimization of MEMS capacitive accelerometer.*Microsystem Technologies*, 19:713–720, 2013. doi: 10.1007/s00542-013-1741-z.

[30] Y. Kang and L. Peng. Optimisation design and damping effect analysis of large mass ratio tuned mass dampers. *Shock and Vibration*, 2019(1):8376781, 2019. doi: 10.1155/2019/8376781.

[31] M.H. Chu and K. Hane. Design, fabrication and vacuum operation characteristics of two-dimensional comb-drive micro-scanner. *Sensors and Actuators A: Physical*, 165(2):422–430, 2011. doi: 10.1016/j.sna.2010.11.004.

[32] S. Khan and G.K. Ananthasuresh. Improving the sensitivity and bandwidth of in-plane capacitive microaccelerometers using compliant mechanical amplifiers. *Journal of Microelectromechanical Systems*, 23(4):871–887, 2014. doi: 10.1109/JMEMS.2014.2300231.

[33] S. Łuczak, R. Grepl, and M. Bodnicki. Selection of MEMS accelerometers for tilt measurements. *Journal of Sensors*, 2017(1):9796146, 2017. doi: 10.1155/2017/9796146.